P34

The Hard X-rays and Gamma-rays from Solar Flares

James M. McTiernan[1]

and

Vahé Petrosian[2]

November 1989

[1]Current Address, Space Sciences Lab, University of California

[2]Department of Applied Physics, Stanford University

National Aeronautics and Space Administration Grant NSG 7092

National Science Foundation Grant ATM 8320439

ABSTRACT

Radiation of energies from 10 keV to greater than 10 MeV has been observed during solar flares, and is interpreted to be due to bremsstrahlung by relativistic electrons. A complete treatment of this problem requires solution of the kinetic equation for relativistic electrons and inclusion of synchrotron energy losses. Using the elctron distributions obtained from numerical solutions of this equation the bremsstrahlung spectra in the impulsive X-ray and γ-ray regimes are calculated, and the variation of these spectral indices and directivities with energy and observation angle are described. The dependences of these characteristics of the radiation of changes in the solar atmospheric model, including the convergence of the magnetic field, the injected electron spectral index, and most importantly, in the anisotropy of the injected electrons and the of convergence of the magnetic field are also described. The model results are compared with stereoscopic observations of individual flares and the constraints that this data sets on the models are discussed. *Subject headings:* Sun:flares–Sun:X-rays–X-rays:spectra–radiation mechnanisms

I. Introduction

It is generally accepted that the hard X-rays and continuum γ-rays from impulsive solar flares are due to bremsstrahlung radiation from non-thermal electrons. The characteristics of the radiation such as the spectrum, directivity, polarization and spatial structure depend on the properties of the accelerated electrons and the geometry of the magnetic field. Consequently observed radiation can give information about the distribution of the accelerated electrons and the magnetic field structure during the impulsive phase. For this purpose we have developed programs to calculate the radiation expected from models with different distributions of accelerated electrons and magnetic field structures. The comparisonsof the model results with observations constrain the models.

Using a steady state Fokker-Planck equation described by McTiernan and Petrosian (1989), hereafter referred to as Paper I, we have calculated for many models the electron flux $F(E, \mu, s)$, where E is the kinetic energy, μ is the pitch angle cosine, and s is the distance from the injection point along the field lines (cf. Paper I). In this paper we shall describe the calculation of the spectral characteristics of the bremsstrahlung radiation from the non-thermal electrons. This work is an extension of earlier work by Leach and Petrosian (1983) on X-ray radiation to emission of γ-rays by relativistic electrons.

Observations of impulsive phase radiation in regard to its directionality have been difficult and the results somewhat controversial. There exist two kinds of observations. The stereoscopic observations carried out by Kane and his collaborators using the ISEE-3 (or ICE) and PVO satellites provide the most direct method of determining the isotropy of impulsive hard X-rays and γ-rays from 100 keV to 1 MeV, (Kane *et al.* 1988). However, at present there have been very few observations of strong flares from two largely separated directions. The second kind of observations relies on statistical variation of radiation characteristics such as rate of occurrence, burst intensity and spectral characteristics with flare position on the solar disk (i.e., observed disk to limb variations). The first such study, using observations from the OSO-7

satellite, was described by Datlowe *et al.* (1974) and analyzed by Petrosian (1975) and Datlowe *et al.* (1977). These observations of low energy hard X-rays show little evidence of anisotropy in agreement with the theoretical models of Leach and Petrosian (1983). The more recent observations from SMM also show similar results in the X-ray regime. This picture changes gradually with increasing energy; the anisotropy of the radiation appears to increase leading to the dramatic concentration of flares with $>$ 10 MeV emission near the solar limb (Riger *et al.* 1984). The statistical behavior of the anisotropy in the γ-ray regime obtained from GRS on SMM is described by Vestrand *et al.* (1987) and Bai (1988). This gradual change is evident in most of the model results and, as pointed out by Petrosian (1985), can be understood in terms of the decrease with energy of collisional pitch angle diffusion.

In this Paper we concentrate on spectral variation with the viewing angle of non-thermal thick target models. The calculation of the bremsstrahlung radiation is discussed in Section II along with the parameters of the assumed model atmosphere and field geometry of the flare region. In Section III we describe the variation of the emitted radiation with observation angle, position within the flare loop and photon energy for models with different accelerated electron energy and pitch angle distributions, and different degrees of convergence of the magnetic field. The results are compared with the stereoscopic observations of flares presented by Kane *et al.* (1988) in Section III. In Section IV we summarize our results. In a third paper of this series we compare the model results with the observed disk to limb variations.

II. Calculation of Bremsstrahlung Emission

In order to get the radiation from an electron distribution we must integrate the product of the electron flux with the bremsstrahlung cross section. We follow the procedure described in Leach (1984) to evaluate the Stokes parameters, which are extensively discussed in the literature. [See e.g., Haug (1972) or Bekefi (1966).] The Stokes parameters are then used to calculate the spectrum and polarization of the radiation.

The radiation is linearly polarized due to the reflective symmetry around the

plane of the photon and incident electron momenta. In this paper we will describe the spectrum and directivity but not the polarization of the radiation. The photon flux as a function of the photon energy k, and polar and azimuthal angles θ and ϕ is obtained from

$$J(k,\theta,\phi,s) = \qquad n(s)\int_0^\infty dE \int_0^\pi d\Theta \int_{-\pi}^{\pi} d\Phi \sigma(k,E,\Theta)F(E,\mu,s)\ , \qquad (1)$$

where $n(s)$ is the density of nuclei and ions, and Θ and Φ are the polar and azimuthal angles of the electron momentum with respect to the photon direction $\hat{\mathbf{k}}$. As described in Paper I electrons are tied to the field lines so that the electron flux may be expressed in terms of the electron energy E, pitch angle cosine μ and distance along the field line s. The cross section σ is the sum of the cross sections for parallel and perpendicular polaraizations. It will not be reproduced here, but may be found in Koch and Motz (1959), equation (2BN).

The electron pitch angle cosine μ is a complex function of the angles Θ, Φ, θ and ϕ. For comparison with observations it is convenient to express the photon flux relative to a coordinate system fixed at the surface of the sun with the z axis in the radial direction. The polar angle θ of the photon then corresponds to the heliocentric angle of the flare; $\theta = 0$ for a flare at the center of the disk, and $\theta = 90°$ for a flare on the limb. The pitch angle cosine is given by

$$\mu = \cos\theta_e \cos\theta_B + \sin\theta_e \cos\phi_e \sin\theta_B\ , \qquad (2)$$

where θ_B is the angle of the magnetic field with respect to the z-axis,

$$\cos\theta_e = \cos\theta\cos\Theta - \sin\theta\sin\Theta\cos\Phi$$

and

$$\phi_e = \phi + \tan^{-1}\left[\frac{\sin\Theta\sin\Phi}{\cos\theta\sin\Theta\cos\Phi + \sin\theta\cos\Theta}\right]\ . \qquad (3)$$

Given the variation along the magnetic field line of the density $n(s)$ and the variation of the angle of the magnetic field with respect to the z axis, $\theta_B(s)$, then the flux in any direction may be found as a function of distance s from the above equations.

For the field variation we assume a magnetic loop consisting of a semicircular coronal portion with vertical footpoints below the transition region.

Since the available observations of directivity are spatially unresolved we need the integral over depth of the photon flux, given by

$$J(k,\theta,\phi) = (4\pi r_o^2 \ln\Lambda)^{-1} \int_0^\infty dE \int_0^\infty d\tau_c \int_0^\pi d\Theta \int_{-\pi}^\pi d\Phi \sigma F(E,\mu,\tau_c) \ , \qquad (4)$$

where τ_c is the dimensionless column depth defined in Paper I; $d\tau_c = 4\pi r_o^2 n(s) \ln\Lambda ds$, r_o is the classical electron radius, and $\ln\Lambda \approx 20$ for a fully ionized ambient plasma.

Most of the radiation, especially at higher energies, comes from the footpoints below the transition region where the magnetic field is vertical. Hence most of the radiation will be azimuthally symmetric and depend only on the polar angle. The small amount of low energy radiation from the coronal part of the loop could be azimuthally asymmetric and could affect the center to limb variation of the radiation, depending on the position and orientation of the loop with respect to the solar equator. For example, for a loop straddling the equator, and the angle of the projection of the loop on the disk is $\pi/2$, there is no azimuthal asymmetry throughout the loop, while if the angle is less than $\pi/2$, the emission from the coronal portion will be asymmetric and the overall center to limb variation will be slightly different than that of the vertical part. In what follows we shall ignore this small dependence and use the azimuthally averaged photon flux

$$J(k,\theta) = (2\pi)^{-1} \int_0^{2\pi} J(k,\theta,\phi) d\phi \ . \qquad (5)$$

Finally we define the average flux

$$J(k) = \frac{1}{2} \int_0^\pi J(k,\theta) \sin\theta d\theta \qquad (6)$$

which will be useful especially for low energies where the bremsstrahlung emission is nearly isotropic.

The evaluation of the electron flux $F(E,\mu,\tau_c)$ and the integrations in equations (1) and (4) require, in addition to $\theta_B(s)$ and $n(s)$, the knowledge of the variation of the strength of the magnetic field (actually the logarithmic derivative $d\ln B/ds$) and plasma

density $n(s)$ along the field lines. These are obtained from the solar atmospheric models which will be the same as those discussed in Paper I. In Figure 1 we show the variation with hieght of the density n, temperature T and column depth N from the top of the loop. Note that the atmospheric model prescribes variation with hieght, not s. Below the transition region, because of our assumption of vertical field lines, the two variations are identical. This is true for density and temperature in the corona as well because these quantities are constant there. The variation with s of column depth, however, depends on the radius of the loop or the length of the loop to the transition region $s_{\rm tr}$.

We assume a pure hydrogen atmosphere; the addition of heavier elements renormalizes the results but has no effect on the angular or spectral variation of the radiation. The level of ionization of hydrogen is computed using the Saha equation and the temperature profile given in Figure 1. In the corona the plasma is fully ionized. The ionization level decreases with temperature, and the plasma is mostly neutral below the transition region. As shown in Paper I, the level of ionization can have some effect on the angular distribution of the electron flux so it might affect the angular variation of the radiation.

In Figure 1 we show two possible variations for the magnetic field. In one it is assumed, as in Leach and Petrosian (1983), that $S_b \equiv d\ln B/ds$ is constant, so that most of the convergence of the field occurs in the corona. Since most of the high energy radiation comes from the footpoints, from the electrons that escape the corona, we call this a "precipitation" model. In the second kind of model we assume $d\ln B/d\ln n$ = constant, so that the field is constant in the corona but increases as some power of the density (or pressure, since T is nearly constant) below the transition region; $B \propto n^{\epsilon}$. This kind of convergence, which we call the "trap" model, may have a more significant effect and is similar to the models of MacKinnon and Brown (1988) and Miller and Ramaty (1989).

We note, however, that a complete knowledge of the variation of $B(s)$ and $n(s)$ is not always needed. As can be seen from equation (4), for analysis of spatially unresolved observation the knowledge of $n(s)$ is not necessary. Similarly, as shown in Paper I, for a

flare the synchrotron losses are important only for very high energies and if the magnetic field in the corona exceeds 10^4 G. If we ignore synchrotron losses we need only to specify the value of $d\ln B/d\tau_c$ for a complete description of the problem and not $B(s)$ and $n(s)$ separately. For precipitation models most of the convergence is in the corona and whether it influences the electron distribution depends on whether $b_T \equiv B(s_{\rm tr})/B_o$ is greater than one. We specify this function which is directly related to the parameter $d\ln B/d\tau_c$ given the coronal density $n_o = 10^{10}{\rm cm}^{-3}$ and the depth of the transition $s_{\rm tr} = 2.4 \times 10^4$ km. For the "trap" models, the most important paramter is ϵ but in practice, since the numerical integration can only be extended to a finite column depth $N_{\rm max}$, we specify the ratio $B(N_{\rm max})/B_o$ from which we evaluate ϵ. We choose $N_{\rm max} = 6 \times 10^{25}$ cm^{-2} which corresponds to $\tau_c \approx 650$ at which point the vast majority of electrons with energies $\lesssim 100$ MeV have disappeared.

As in Paper I we assume injected fluxes with power law energy spectra and isotropic or gaussian pitch angle distributions, with maxima at pitch angle α_1 ($\alpha_1 = 0$ for "beam" models or $\alpha_1 = \pi/2$ for "pancake" models) and dispersion α_o^2:

$$F(E,\mu,0) = 2KE^{-\delta}\alpha_o^{-2}e^{-(\alpha-\alpha_1)^2/\alpha_o^2} \ . \tag{7}$$

where small values of α_o^2 imply highly beamed or flattened distributions and $\alpha_o^2 \to \infty$ implies an isotropic distribution. The total number of electrons with energy greater than E_o is then $KE_o^{1-\delta}/(\delta-1)$.

III. Characteristics of Radiation

The characteristics in which we are interested here are the directivity (variation with θ and ϕ) and the spectrum (variation with k) of the bremsstrahlung radiation. For comparison with spatially resolved observations we need in addition these chararcteristics as functions of depth s along the field lines, namely $J(k,\theta,\phi,s)$. There are, however, very few reliable spatially resolved observations, especially at high energies. Spatially resolved observations by HXIS or Hinotori were primarily at low energies and sometimes suffered from contamination from the thermal component. The only information on the spatial structure at higher energies has come from

limb occulted flares (Kane 1982) which were analyzed by Brown *et al.* (1981) and Leach and Petrosian (1983). Consequently, we shall leave a complete description of depth dependence of emission for all models to the future if and when data becomes available from Max '91 missions. For now we concentrate on the spatially integrated characteristics and their comparison with existing observations. However, in order to clarify some aspects of the spatially integrated results we present the characteristics of emission as functions of depth for one model.

A. Dependences on Depth

For this purpose we select the model, which will be called the standard model, with an isotropic injected pitch angle distribution ($\alpha_o^2 = \infty$) and a uniform magnetic field ($d\ln B/ds = 0$). We shall be concerned with field strengths and energies such that the synchrtron losses are negligible and the problem can be formulated in terms of the column depth $\tau_c = N/N_o$, where $N_o = 5 \times 10^{22}$. As shown by Leach (1984) (see also Canfield *et al.* 1985 or Brown and McClymont 1975) for non-relativistic energies the dependence of the bremsstrahlung intensity on depth scales very simply with energy. He found that the fractional emission integrated over all angles, $I(k,\tau_c) \equiv J(k,\tau_c)/J(k)$, is proportional to $(k^2 + \tau_c)^{-\delta/2}$. The logarithmic plots of I versus τ_c are very similar to the plots of the electron flux integrated over pitch angle $F_\mu(E,\tau_c)$ versus τ_c shown in Figure 5 of Paper I. In Figure 2a we show the variation of $\tau_c I$ with τ_c. We have multiplied I by τ_c in order to show from where, on this logarithmic plot, most of the emission originates. As evident from the figure this happens when the curves reach their maxima at $\tau_c \approx \eta(k) \equiv k^2/(k+1)$. The simple scaling found by Leach (1984) gradually breaks down as energy increases.

The actual spatial dependence of the emission depends on the variation of the with depth of the density (for the standard model) and the magnetic field (for the general models). To demonstrate this, in Figure 2b, we show the variation of the fractional emission $I(k,s) = J(k,s)/J(k)$ with depth s. Since $d\tau_c/ds \propto n(s)$ these curves behave like the product of $I(k,\tau_c)$ and the ambient density. In the corona, where density is constant and $\tau_c \ll k^2/(k+1)$, $I(k,s)$ is constant. In and below the transition region,

the density increases rapidly, so $I(k,s)$ increases as the density, but eventually beyond $\tau_c = k^2/(k+1)$, $I(k,s)$ begins to decrease because $I(k,\tau_c)$ decreases faster than the increase in density. Thus there is a maximum for fractional emission $I(k,s)$ at the depth corresponding to $\tau_c \approx k^2/(k+1)$, which increases with energy. For $N_{\rm tr} = 2.4 \times 10^{19}$ cm^{-2} as assumed here, for energies greater than $\sim$ 12 keV, the maximum in emission occurs below the transition region, so that the projected image will show two emission regions around the footpoints of the loop. Only for higher column depths $N_{\rm tr}$ and/or lower energies will there be substantial emission from the coronal part of the loop, in which case the geometry and orientation of the loop are important in determining the projected image of the emission. For low coronal density or high energies (gamma rays $\gtrsim$300 keV) these complex geometric factors are absent and the bremsstrahlung emission has azimuthal symmetry so that nnnnthe spatially resolved or integrated emissions depend only on the polar angle θ. We define the total and depth dependent directivities as

$$\Delta(k,\theta) = J(k,\theta)/J(k,90°)\ , \quad \Delta(k,\theta,\tau_c) = J(k,\theta,\tau_c)/J(k,90°,\tau_c)\ , \tag{7}$$

Note that $\theta = 90°$ corresponds to a flare at the limb while $\theta = 0°$ corresponds to a flare at the center of the disk so that the directivity is normalized at the limb. The directivity of the standard model at different depths for 1 MeV emission is shown in Figure 3. First note that even for isotropically injected electrons most of the radiation is directed towards the photosphere ($90 < \theta < 180°$), and only a small fraction is directed into the observable hemisphere ($0° < \theta < 90°$), especially at larger depths. In general, for a given model, the qualitative behavior of the directivity is the same as that of the electron pitch angle distribution, but the anisotropy in the radiation distribution is smaller than that for the electron distribution, since the cross-section has a finite width.

Figure 4 gives the normalized photon spectrum $J(k,s)k^{\delta-1}$ versus energy k for limb flares ($\theta = 90°$) at different depths. The curves labeled **corona**, **Photosphere** and 90 represent the spectra for emission from the corona, photosphere and whole loop, respectively. In the corona the spectra are steeper because the higher energy electrons emit mostly at lower depths. The spectra become flatter with increasing depth, and at

the photosphere the spectral indicies are less than $\delta - 1$, which is the appropriate value of the spectral index for the emission from the whole loop.

B. Characteristics of Unresolved Emission

The spatially unresolved observations can be dealt with by consideration of the variation of the emission from the whole loop with photon energy k and observation angle θ which is given by the flux $J(k, \theta)$ and the directivity $\Delta(k, \theta)$. Te general behavior of these quantities is demonstrated by the dashed lines marked 0 and 60 and the solid line marked 90 in Figure 4. The spectra become flatter going from $\theta = 0°$ to $\theta = 90°$ (center to limb) but are all steeper than the curve for the total emission (the dashed line labeled `Total`), which includes emission for angles greater than 90°, directed into the sun. This is a consequence of the change in anisotropy with energy depicted in Figure 5 which shows $\Delta(k, \theta)$ versus θ for energies 16 keV, 300 keV, 1 MeV, and 10.6 MeV. As expected the range of the directivity increases with energy. Most of the variation in the directivity occurs between 60° and 90°. The statistical evidence for such changes of spectral index with angle has been observed (Vestrand *et al.* 1987). Since the magnitude of the change is model dependent, such observations should enable us to put constraints on models. This will be the subject matter of our third paper of this series.

The spectra can not be described well single power laws since the curves steepen or flatten as the energy increases. We describe this behavior by fitting the photon flux to power laws in three regimes and obtain the spectral indices γ_x for 16 to 210 keV, γ_m for 300 keV to 1 MeV, and γ_γ for 2.6 to 21.2 MeV. The breaks in the spectra, i.e., the differences between the spectral indices in different energy ranges, are also dependent on angle, and the way they change with angle is model dependent. We will discuss these dependences in the following section.

Note that the total spectrum integrated over all angles has indices $\gamma_x \approx \delta - 1$, $\gamma_m \approx \delta - 1$ and $\gamma_\gamma \lesssim \delta - 1$; the total spectrum flattens slightly for extreme relativistic enegies. This is generally true for all of the models, and is due to the fact that collisions are the dominant loss process. We can find this result easily using the non-relativistic and relativistic limits for the bremsstrahlung cross section integrated over all angles

[equations 3BN(a) and (b) from Koch and Motz (1959)], and by assuming that the electron flux is completely isotropic with the energy dependence given by equation (28) of Paper I; i.e.,

$$F_{\rm TOT}(E) = \propto \begin{cases} E^{-(\delta-2)} & \text{for } E \ll m_e c^2 \\ E^{-(\delta-1)} & \text{for } E \gg m_e c^2 \end{cases} . \tag{8}$$

We may then integrate the product of flux and cross section over energy, and we find

$$J_{\rm TOT}(k) \propto \begin{cases} k^{-(\delta-1)} & \text{for } k \ll m_e c^2 \\ k^{-(\delta-1)} \ln(k/m_e c^2) & \text{for } k \gg m_e c^2 \end{cases} . \tag{9}$$

The relativistic regime has a slightly flatter spectrum due to the logarithmic dependence on energy. We now consider the effects of variation of the model parameters.

1. Plasma Density Profile and Ionization Level

The ratio of bremsstrahlung emission rate to collisional energy loss rate is fairly independent of the density and varies slightly with the ionization state of the plasma. Consequently, when collisions are dominant (synchrotron and other losses are negligible) the emission form unresolved sources is insensitive to the form of the density or ionization profile. This is demonstrated in Figure 5 where the directivity at 1 MeV of the standard model is compared with two models. The dashed line represents the directivity for the model with constant density and full ionization and the o's represent the model with a density profile as shown in Figure 1 which increases from 10^{10}cm^{-3} in the corona to 10^{18}cm^{-3} at $s = 4300$ km below the transition region, but is fully ionized throughout. There is little difference among these curves, especially for $0° \leq \theta \leq 90°$ which is the range of observable radiation.

2. Electron Spectral Index

The angular variation is also fairly insensitive to the value of the injected spectral index δ. In general the anisotropy of the radiation increases with decreasing values of the spectral index of the electrons, but this increase is less than 10% for relavant values of δ (approximately from 2 to 7). The photon spectral index, of course, varies with the

electron spectral index, but the variation with δ of the difference between these two indices,

$$\Gamma_i = \gamma_i - \delta \qquad (i = x, m, \gamma) \tag{10}$$

is in general small.

For the remainder of this paper we shall ignore these differences and, assuming $\delta = 3.75$, discuss the effects of the electron pitch angle distribution parameters α_1, α_o^2 and the convergence of the magnetic field (the parameter $d\ln B/ds$ or the mirror ratio b_T). For each set of parameters we show the dirctivity normalized to unity at $\theta = 90°$ (limb) for observable angles ($0° < \theta < 90°$) and three representative energies, 16 keV, 1 MeV and 10.6 MeV. Similarly we show the variation of the three spectral indices Γ_x, Γ_m and Γ_γ, as defined in equation (10). As we shall see, the general feature of the curves is a hardening (flattening) of the spectra with increasing energy and observation angle.

9. Electron Pitch Angle Distribution

The effects of the injected pitch angle distribution are shown in Figures 6a and 6b. We give results for three models spanning the possible range for the distributions, one highly beamed model ($\alpha_o^2 = 0.04$, $\alpha_1 = 0$, dashed lines), one isotropic ($\alpha_o^2 \to \infty$, solid lines) and one highly flattened pancake model ($\alpha_o^2 = 0.04$, $\alpha_1 = \pi/2$, "-+" lines). As in the standard model, the total anisotropy $\Delta(k, 0°)$, defined as the ratio of emission at 0° to emission at 90°, and the total variation in spectral index, $\Delta\Gamma \equiv \Gamma(0°) - \Gamma(90°)$ increase with energy in all cases. These increases are smallest for the beam injection (dashed lines), and become larger for the isotropic and pancake models model (solid lines and -+ lines, respectively). In each case the gradients are small between 0° and 60° and most of the variation takes place near the limb between 60° and 90°.

As pointed out earlier (Petrosian 1985), this behavior is a consequence of the shape of the cross section, which in general has a maximum at a photon-electron angle $\Theta = 0$ of width $\Delta\Theta \approx m_e c^2/E$, but is fairly flat at large angles. For electron distributions which are beamed along the field lines, the radiation in the range $\theta = 0°$

to 90° is dominated by large angle emission (the flat portion of the cross section) from electrons with small pitch angles. As the width of the electron beam decreases the variation from 0° to 90° decreases, i.e., contrary to naieve expectation the more highly beamed models give more isotropic photon distributions in the observable hemisphere. For the same reason, in the isotropic and pancake models the presence of a large proportion of electrons at high pitch angles results in a larger degree of anisotropy. For emission at lower energies ($k \lesssim 100$ keV) the directivity and spectral index are nearly constant because the cross section does not have the sharp maximum, and the electron distributions are broadened due to collisional diffusion. The anisotropy that does exist (Petrosian and Leach 1983 and Leach 1984) decreases with increasing α_o^2 especially when pancake type distributions are included.

4. Magnetic Field Convergence

Finally, let us consider the effects of non-uniformities in the magnetic field, in particular non-uniformities in the form of loops with field lines which converge monotonically with depth s. As mentioned above we consider two different magnetic field structures. For models with constant $d\ln B/ds$ most of the effects of the convergence occur in the corona, while most of the radiation (especially at high energies) comes from the footpoints, where because of the small density scale height the effect of the convergence is small. The photon and electron distributions are therefore similar to those for the uniform field models except that there are relatively more electrons "backward" hemisphere with pitch angles in the greater than $\pi/2$ (i.e., moving to lower values of s). This is especially true at high energies where the field convergence is much more effective than collisional diffusion in reflecting electrons into the "backwards" hemisphere.

These effects are shown in Figures 7a and 7b where we compare the directivities and spectral indices for the standard model (solid lines) and one with isotropic injection and constant $d\ln B/ds$ with mirror ratio $b_T = B(s_{tr})/B_o = 10$ (dashed lines). The anisotropy and the variation with θ of the spectral indices decrease with increasing convergence. This is a direct result of isotropization of the electron distributions by

the magnetic mirroring process. Note that as in the uniform field models, most of the angular variation takes place between 60° and 90°. This is a characteristic of all the "precipitation" models, i.e., those with field convergence in the corona.

For models with $B(s) \propto (n(s))^{\epsilon}$, there is no convergence in the corona and convergence takes place where the electrons emit most of the radiation. The o's in Figure 7 represent the directivities and spectral indices for a model with mirror ratio $b_T = B(s_{\max})/B_o = 5$. For this type of model the trapping and isotropization become more effective at higher energies and we find that unlike the above models there is significant difference for all angles, and in some cases (for extreme relativistic energies) a significant part of the variation takes place between 0° and 60°.

5. Combined Effects of α_o^2 and $d\ln B/ds$

We have shown the effects of varying α_o^2 for uniform fields and the effects of field convergence for isotropic emission. When both α_o^2 and $B(s)$ are changed, the effects of each variation are combined. It would take a considerable amount of space to present the combined effects graphically. Instead, we summarize the results for the constant $d\ln B/ds$ models and the $B \propto n^{\epsilon}$ in Tables 1 and 2, repectively. In each table values of the total anisotropy from 0° to 90° at 1 MeV, $\Delta(k, 0°)$, and $\Delta\Gamma_i = \Gamma(0°) - \Gamma(90°)$ for in the spectral indices Γ_x, Γ_m and Γ_γ are given for 5 different pitch angle distributions. Note that this does not show shape of the variation with angle, but the values at intermediate angles may be estimated using Figures 6 and 7 as guides.

In Table 1, the largest variation in directivity and spectral index occurs at larger values of field convergence (or b_T) for beamed versus pancake models; it occurs for uniform field for highly pancaked models.

For the $B \propto n^{\epsilon}$ models, shown in Table 2, the behavior is more complex. In general, for a given value of the field convergence (b_T) the disk to limb variation increases from left to right (beam to pancake distributions) with the change becoming negligible at larger values of b_T. For a given value of α_o^2 the change in variation with b_T is largest and in the oppisite direction for highly beamed and pancaked models, except for $\Delta\Gamma_m$, which has essentially the same variation for all α_o^2.

For comparison, observations by the GRS on SMM (Vestrand *et al.* 1987, Bai 1988) show $\langle \Delta\Gamma_m \rangle \approx 0.8$ and $\langle \log(\Delta(1\ \mathrm{MeV}, 0°)) \rangle \approx -1.2$. Inspection of Tables 1 and 2 shows that some values of α_o^2 and b_T can fit this data rather well. Interestingly these include both beam and pancake models but none with isotropic injection. In the next paper we will make a more detailed comparison with these statistical results and will show that beamed models with moderate field convergence are favored.

6. Breaks in Spectra

We have seen that the spectral index changes with energy, and the spectral indices fit for different energies have different angular dependences. For comparison with the data just mentioned, we need to determine the characterisitcs of such spectral breaks. Figure 8 shows the difference between the intermediate and low energy spectral indices, $\gamma_m - \gamma_x$, for the models with constant $d\ln B/ds$ and $b_T = 1$ and 10. A positive (negative) value describes a steepening (flattening) of the spectrum. The converging models show less steepening for all three injected spectra. For both the uniform and converging fields, the change in spectral index is largest for the beam injection, it decreases with increasing width α_o^2 and is smallest for pancake injection. The size of the spectral break also depends on the angle, decreasing with θ for all the models except for the uniform field beam injection. For the uniform field case, the spectrum steepens for the beam and isotropic models over the whole range of θ. The pancake injection shows some flattening at 90°. The size of the break decreases for increasing convergence, and for $b_T = 25$ and pancake injection we see flattening for all values of θ.

The SMM observations mentioned above show that the difference between average spectral indices $\langle \gamma_x \rangle - \langle \gamma_m \rangle$ is about one with no discernable angular variation. None of the models described above can fit this which may indicate that some of our assumptions, in particular, a constant power law spectral index for accelerated electrons, may be incorrect. We shall discuss this this in detail in Paper III.

IV. Comparison with Stereoscopic Observations

We now turn to comparison with the stereoscopic observations of flares made

by Kane *et al.* (1988) leaving a detailed comparison with SMM results to Paper III. Kane *et al.* give photon fluxes and spectral indices for nine large flares observed by detectors on two satellites, the PVO (for Pioneer Venus Orbiter) and ISEE-3 (for Third International Sun Earth Explorer). Ideally one would like use such data to find the range of model parameters which fit each observation. This is not possible for the data in question because of the large error bars. Instead we compare all of the observations with each of the models discussed above (see Tables 2 and 3), to see which of the events fit each model. Examples of such cmoparisons are shown in Figures 9 and 10. The 750 keV fluxes for the two instruments versus angle for the nine events are shown in Figure 9 compared with the flux from the model with the beam injection model with $\alpha_o^2 = 0.40$ and a uniform field. [This choice is motivated by the good agreement that this model shows with SMM results to be discussed in Paper III.] The observed PVO flux is normalized to the model curve at the appropriate angle, and the ISEE-3 flux is shown at its appropriate angle with the same normalization. The error bars are those for the flux ratio $J(\mathrm{ISEE}-3)/J(\mathrm{PVO})$ given by Kane *et al.* The two observed fluxes are connected by dashed lines. Five of the flares fit this model within the uncertainties, two more fit beamed models with smaller values of α_o^2, and two are not close, especially the flare seen near 90° by both instruments. These are the events for which the photon flux index can be larger for the larger angle (including uncertainties). In Figure 10, we make the same comparison using the spectral indices measured by each instrument. The results are similar, but the uncertainties here are larger (to reduce confusion we show some average error bars which are two to three times smaller than the actual observed error bars), and the observations in some cases do not agree with any model or with each other even when the veiwing angles are similar.

Two of the flares cannot be reconciled with the models, all of which predict a larger photon flux and smaller spectral index with increasing θ. In order to fit such flares we must relax our assumptions, in particular the assumption of vertical magnetic fields and a low density corona. The geometric factors that have been ignored may be important. If the magnetic field is not vertical at the footpoints then the viewing angle and the

angle of emission with respect to the field do not correspond to each other and there is no reason to expect the photon flux to increase with increasing observation angle.

V. SUMMARY

We have described the angular variation of bremsstrahlung radiation with observation angle and discussed the effects of different injected distributions and magnetic field structures. We find that our models fit some stereoscopic observations of real flares, but find it difficult to constrain the flare parameters using these comparisons. Taken at face value, this comparison for some flares it seems to imply that our assumption that the magnetic field is vertical at the footpoints, and that the electrons are accelerated in the corona may not be correct. However, due to the observational uncertainties in the data such a conclusion is not warranted yet. In a subsequent paper we shall compare with some observations which fit the models much better, and give us a reason to believe that our assumptions are correct.

Acknowledgements

We would like to thank E.T. Lu, R.J. Hamilton and S.R. Kane for valuable discussions and information. This work was supported by the National Aeronautics and Space Administration under grant NSG-7092 and by the National Science Foundation under grant ATM 8320439.

References

Bai, T. 1988, *Ap. J.*, **334**, 1049.

Bekefi, G. 1966, *Radiation Processes in Plasmas*, Wiley, New York.

Brown, J.C. and McClymont, A.N. 1975, *Solar Phys.*, **41**, 135.

Brown, J.C., Hayward, J. and Spicer, D.F. 1981, *Ap. J. (Letters)*, **245**, L91.

Canfield, R.C., Bely-Dubau, F., Brown, J.C., Dulk, G.A., Emslie A.G., Ohki, K., Enome S., Gabriel A.H., Kundu M.R., Melrose D.B., Neidig, D.F., Petrosian, V. , Poland A., Rieger E., Tanaka K. and Zirin H. 1985, *Impulsive Phase Transport*, Chapter 3 of *Energetic Phenomena on the Sun*, Eds. M.R. Kundu and B. Woodgate, NASA Conference Publication **2439**.

Datlowe, D.W., Elcan, M.J. and Hudson, H.S. 1974, *Solar Phys.*, **39**, 155.

Datlowe, D.W., O'Dell, S.L., Peterson, L.E and Elcan, M.J. 1977, *Ap. J.*, **212**, 561.

Haug, E. 1972, *Solar Phys.*, **25**, 425.

Kane, S.R., Fenimore, E.E., Klebesadel, R.W. and Laros, J.G. 1988, *Ap. J.*, **326**, 1017.

Koch, H.W. and Motz J.W. 1959, *Rev. Mod. Phys.*, **31**, 920.

Leach, J. and Petrosian, V. 1983, *Ap. J.*, **269**, 715.

Leach, J. 1984, Ph.d. Thesis, Stanford University.

Leach, J. , Emslie, A.G. and Petrosian, V. 1985, *Solar Phys.*, **96**, 331.

MacKinnon, A.L. and Brown, J.C., 1988, Preprint.

McTiernan, J.M. and Petrosian, V. , 1918, in preparation.

Miller, J.A. and Ramaty R., 1989, Preprint.

Petrosian, V. 1975, *Ap. J.*, **197**,235.

Petrosian, V. 1985, *Ap. J.*, **299**,987.

Riger, E., Reppin, C., Kanbach, G., Forrest, D.J., Chupp, E.L. and Share, G.H. 1984, 18th International Cosmic Ray Conference, **4**, 79.

Vestrand, W.T., Forrest , D.J., Chupp, E.L., Riger, E., and Share, G.H. 1987, *Ap. J.*, **322**, 1010.

Table 1

Anisotropy $D(k) = \Delta(k, 0°)$ at 1 MeV, the difference in spectral indices from 0° to 90°, $\Delta\Gamma = \Gamma(0°) - \Gamma(90°)$ for Γ_x, Γ_m and Γ_γ, for the constant $d\ln B/ds$ models, for four values of the mirror ratio b_T and five values of α_o^2. Beam injection is denoted by a (b), and pancake injection is denoted by a (p).

log[D(1 MeV)]

$b_T \backslash \alpha_o^2$	0.04(b)	0.40(b)	∞	0.40(p)	0.04(p)
1.0	−0.93	−1.29	−1.72	−1.91	−2.14
2.5	−1.28	−1.73	−1.74	−1.73	−1.65
10.0	−1.65	−1.60	−1.50	−1.39	−1.26
25.0	−1.57	−1.39	−1.27	−1.08	−0.95

$\Delta\Gamma_x$ (16 to 210 keV)

$b_T \backslash \alpha_o^2$	0.04(b)	0.40(b)	∞	0.40(p)	0.04(p)
1.0	0.39	0.50	0.64	0.73	0.81
2.5	0.48	0.63	0.68	0.70	0.71
10.0	0.61	0.63	0.60	0.56	0.52
25.0	0.61	0.54	0.48	0.38	0.32

$\Delta\Gamma_m$ (300 keV to 1 MeV)

$b_T \backslash \alpha_o^2$	0.04(b)	0.40(b)	∞	0.40(p)	0.04(p)
1.0	0.26	0.65	1.16	1.33	1.62
2.5	0.70	1.22	1.22	1.21	1.15
10.0	1.15	1.15	1.11	1.06	0.97
25.0	1.11	1.05	1.01	0.92	0.84

$\Delta\Gamma_\gamma$ (2.6 to 21.2 MeV)

$b_T \backslash \alpha_o^2$	0.04(b)	0.40(b)	∞	0.40(p)	0.04(p)
1.0	0.60	0.80	1.47	1.49	1.73
2.5	1.76	1.18	1.02	0.94	0.86
10.0	1.12	0.94	0.88	0.84	0.81
25.0	0.88	0.75	0.71	0.70	0.68

Table 2

Same as Table 1 for the models with $B(s) \propto [n(s)]^{\epsilon}$. Here there are three values of the mirror ratio b_T.

$\log[D(1\ \text{MeV})]$

$b_T \backslash \alpha_o^2$	0.04(b)	0.40(b)	∞	0.40(p)	0.04(p)
1.0	−0.93	−1.29	−1.72	−1.91	−2.14
2.5	−1.46	−1.90	−1.97	−2.00	−2.00
5.0	−1.75	−1.87	−1.88	−1.89	−1.88

$\Delta\Gamma_x$ (16 to 210 keV)

$b_T \backslash \alpha_o^2$	0.04(b)	0.40(b)	∞	0.40(p)	0.04(p)
1.0	0.39	0.50	0.64	0.73	0.81
2.5	0.43	0.60	0.66	0.71	0.73
5.0	0.50	0.60	0.63	0.67	0.66

$\Delta\Gamma_m$ (300 keV to 1 MeV)

$b_T \backslash \alpha_o^2$	0.04(b)	0.40(b)	∞	0.40(p)	0.04(p)
1.0	0.26	0.65	1.16	1.33	1.62
2.5	0.99	1.44	1.50	1.52	1.52
5.0	1.35	1.45	1.45	1.45	1.46

$\Delta\Gamma_\gamma$ (2.6 to 21.2 MeV)

$b_T \backslash \alpha_o^2$	0.04(b)	0.40(b)	∞	0.40(p)	0.04(p)
1.0	0.60	0.80	1.47	1.49	1.73
2.5	2.22	2.06	2.02	2.02	2.03
5.0	2.07	2.02	2.02	2.01	2.01

Figures

Figure 1: The logarithmic variation with height above the transition region of the magnteic field and plasma; n_{10} is the tootal density in units of 10^{10}cm^{-3}, N_{19} is the column depth in units of 10^{19} cm^{-2}, T is the temperature, B_p and B_t are the magnetic field for two models: for B_p, $d\ln B/ds$ = constant, and for B_t, $B \propto n^{0.2}$.

Figure 2: Fractional emission, (a) $\tau_c I(k,\tau_c)$ versus normalized column depth τ_c, (b) $I(k,h)$ versus height h for 5 keV, 16 keV, 300 keV, 1 MeV, and 10.6 MeV emission for isotropic injection and uniform field. Each curve is labeledby the photon energy in MeV.

Figure 3: Directivity $\Delta(k,\theta,\tau_c)$ versus observation angle θ at different depths at 1 MeV for the isotropic injection, uniform field model. Each curve is labeled with the appropriate value of $\tau_c/\eta(k)$. The curve labeled `Total` is the directivity for the whole loop, $\Delta(k,\theta)$

Figure 4: Photon fluxes (multiplied by $k^{\delta-1}$) versus energy k. The solid curves labeled `corona`, `photosphere` and 90 represent $J(k,\theta,\tau_c)$, the emission integrated over τ_c for the corona, photosphere and the whole loop for a limb flare ($\theta = 90°$). The dashed lines represent $J(k,\theta)$, the emission from the whole loop, for $\theta = 0°$, 60°, and the curve labeled `Total` represents $J(k)$, the emission integrated over all angles.

Figure 5: Directivity $\Delta(k,\theta)$ versus observation angle θ for the isotropic injection and uniform field model. Each curve is labeled by the value of the photon energy in MeV. The dahsed line represents the 1 Mev directivity for a model with constant density and fully ionized plasma and the o's represent a model with density increasing in depth, but also fully ionized.

Figure 6: (a) Directivity versus observation angle for emission at 16 keV, 1 MeV and 10.6 MeV for uniform magnetic field models. The solid lines denote isotropic

injection, dashed lines denote beam injection with $\alpha_o^2 = 0.04$, and the "-+" lines denote pancake injection with $\alpha_o^2 = 0.04$. (b) Same as (a) for the spectral indices Γ_x (shifted down by 1.0), Γ_m (not shifted) and Γ_γ (shifted up by 1.0). The curves are labeled by the range in energy for the spectral indices.

Figure 7: Same as Figure 6 for isotropic injection models with uniform field (solid lines) constant $d\ln B/ds$ with $b_T = 10$ (dashed lines) and $B \propto n^{0.2}$ (o's)

Figure 8: The break in the spectral index $\Gamma_m - \Gamma_x$ for models with constant $d\ln B/ds$ and $b = 1$ and 10. The solid lines denote isotropic injection, dashed lines denote beam injection with $\alpha_o^2 = 0.40$, and the "-+" lines denote pancake injection with $\alpha_o^2 = 0.40$. The upper curve for each case is the uniform field model, the lower one the converging field model.

Figure 9: A comparison of stereoscopic observations of photon flux at 750 keV from the PVO and ISEE-3 spacecraft with numerical results. The curve is the directivity versus θ for the model with beam injection of width $\alpha_o^2 = 0.40$ and a uniform magnetic field. The open circles are the PVO fluxes normalized to the numerical results, and the circles with error bars are the normalized values of the ISEE-3 photon fluxes the two observations for each event are connected by dashed lines. The filled circles represent the events for which no models fit.

Figure 10: Same as Figure 9 for the spectral indices γ_p and γ_I.

Figure 1

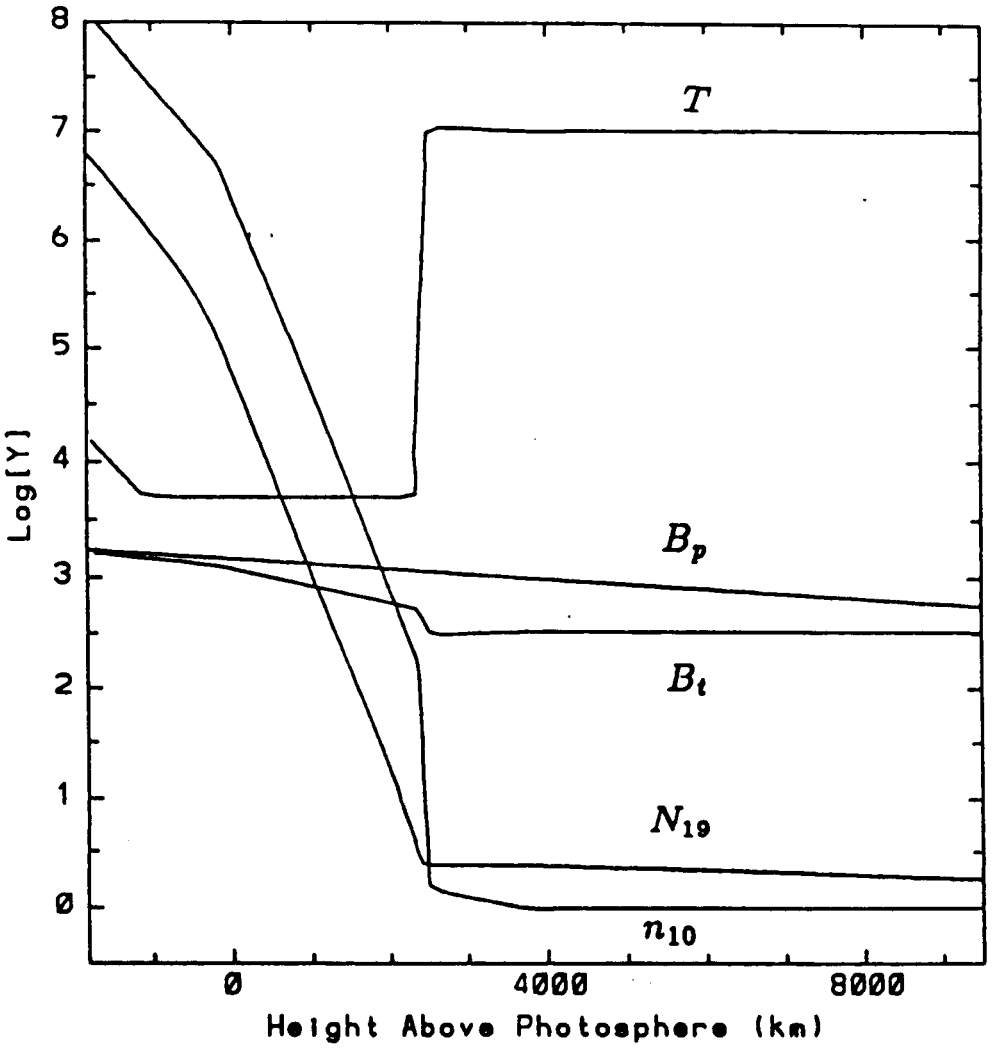
8
7
6
5
4
3
2
1
0
Log[Y]
T
B_p
B_t
N_{19}
n_{10}
0
4000
8000
Height Above Photosphere (km)

Figure 2

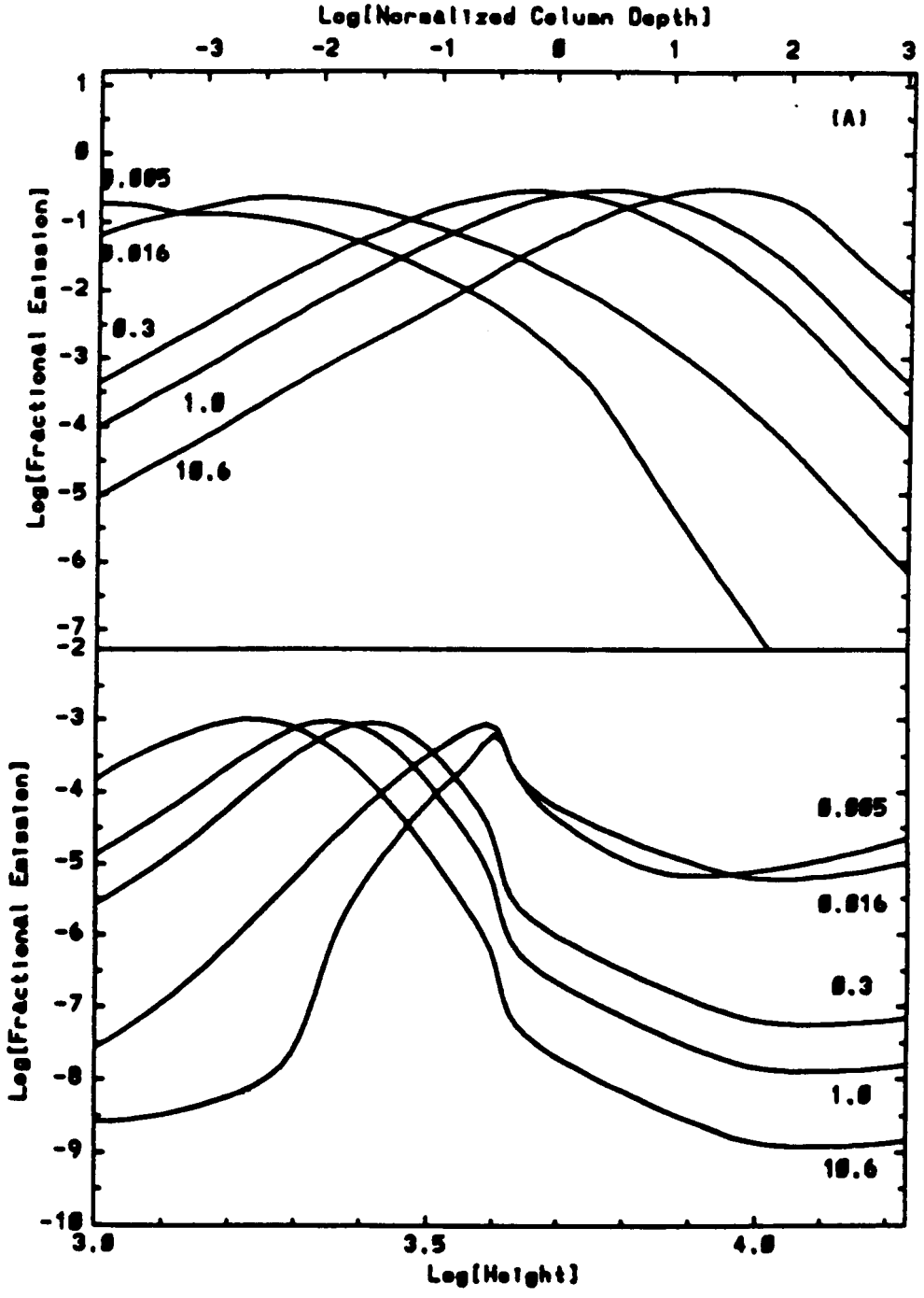
Log[Normalized Column Depth]
-3
-2
-1
0
1
2
3
(A)
0.005
0.016
0.3
1.0
10.6
Log[Fractional Emission]
Log[Fractional Emission]
0.005
0.016
0.3
1.0
10.6
3.0
3.5
4.0
Log[Height]

Figure 3

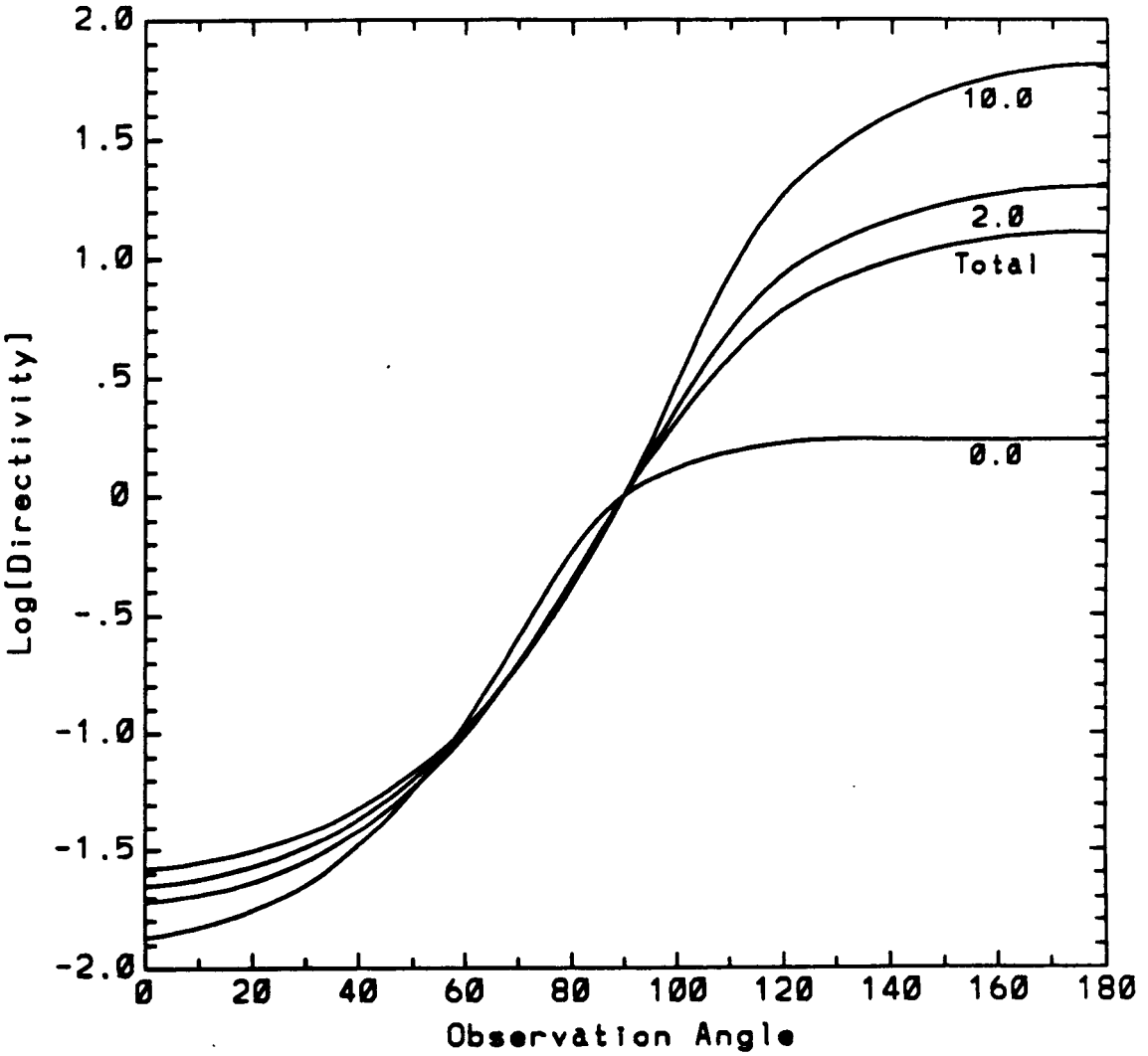
2.0
1.5
1.0
.5
0
-.5
-1.0
-1.5
-2.0
Log[Directivity]
0
20
40
60
80
100
120
140
160
180
Observation Angle
10.0
2.0
Total
0.0

Figure 4

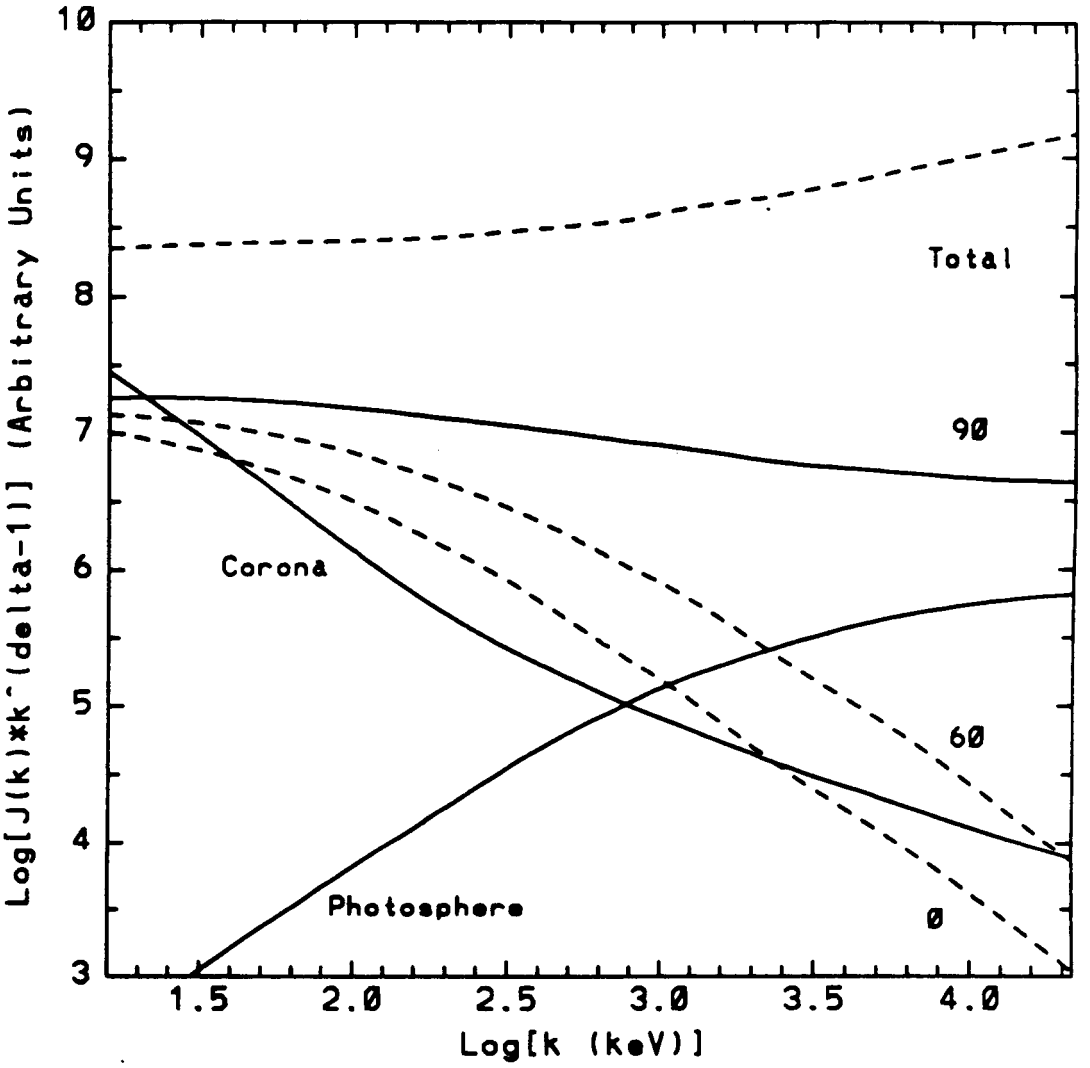
10
9
8
7
6
5
4
3
1.5
2.0
2.5
3.0
3.5
4.0
Log[J(k)*k^(delta-1)] (Arbitrary Units)
Log[k (keV)]
Total
90
60
0
Corona
Photosphere

Figure 5

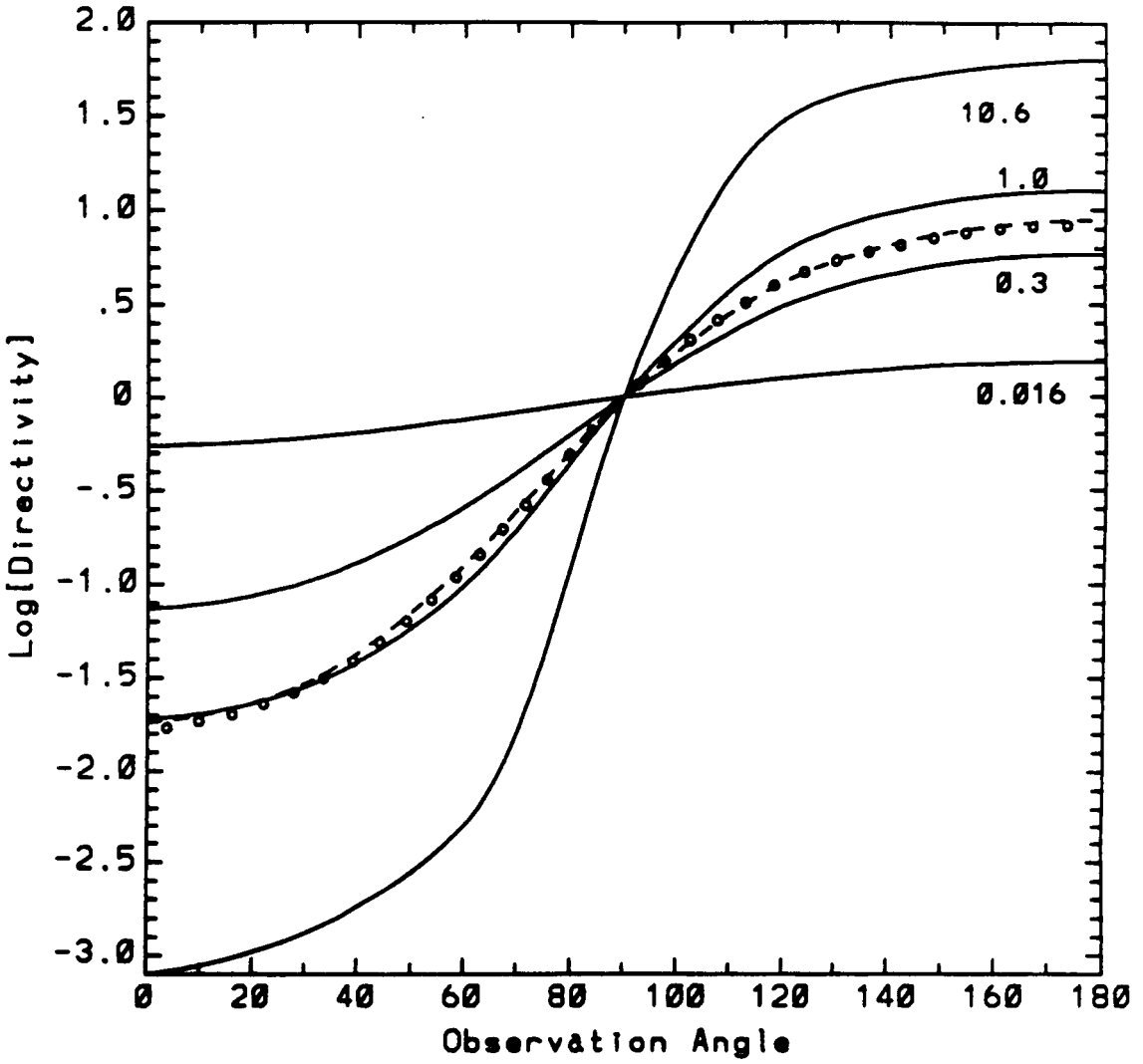
2.0
1.5
1.0
.5
0
-.5
-1.0
-1.5
-2.0
-2.5
-3.0
Log[Directivity]
0
20
40
60
80
100
120
140
160
180
Observation Angle
10.6
1.0
0.3
0.016

Figure 6

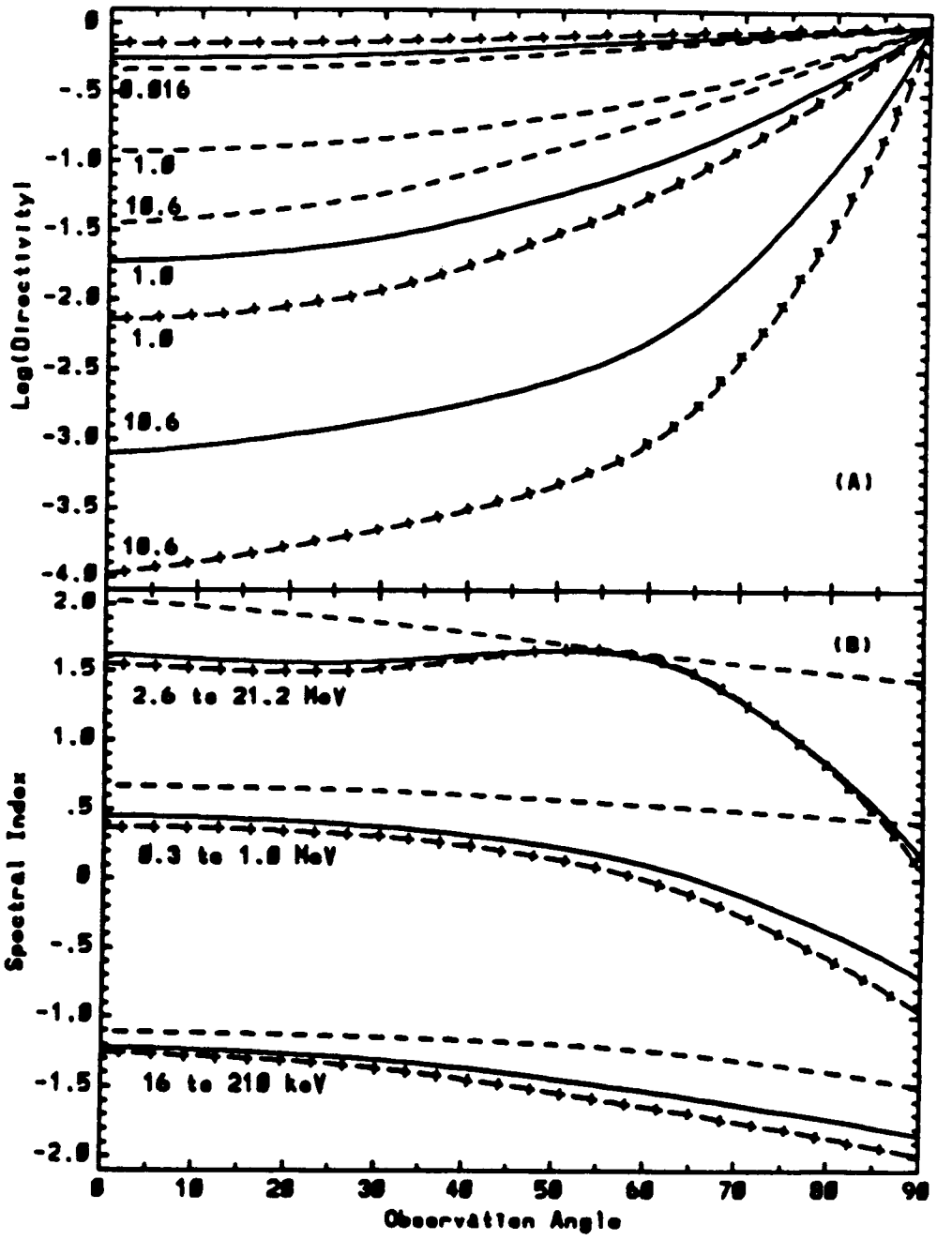

Figure 7

ORIGINAL PAGE IS
OF POOR QUALITY

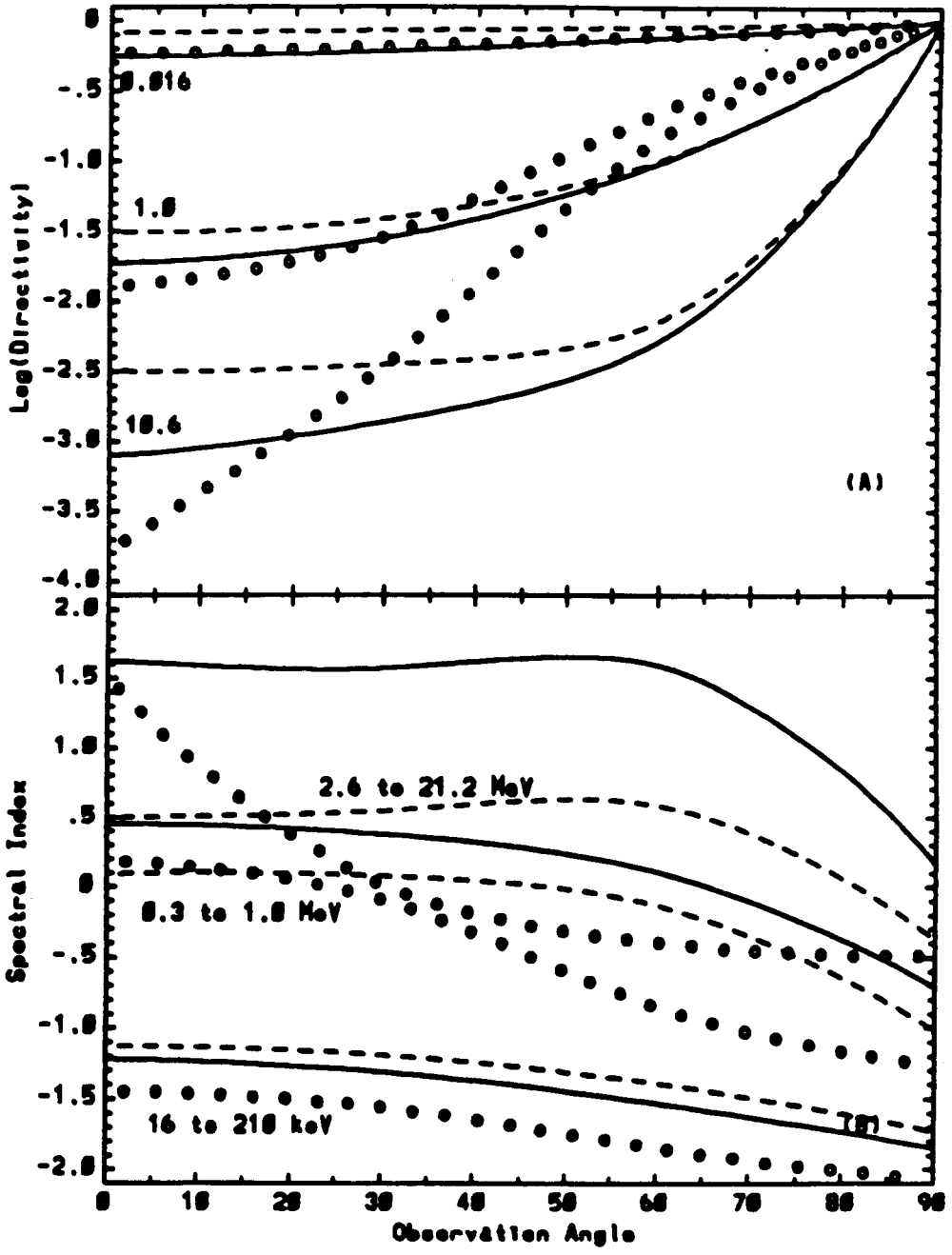

Figure 8

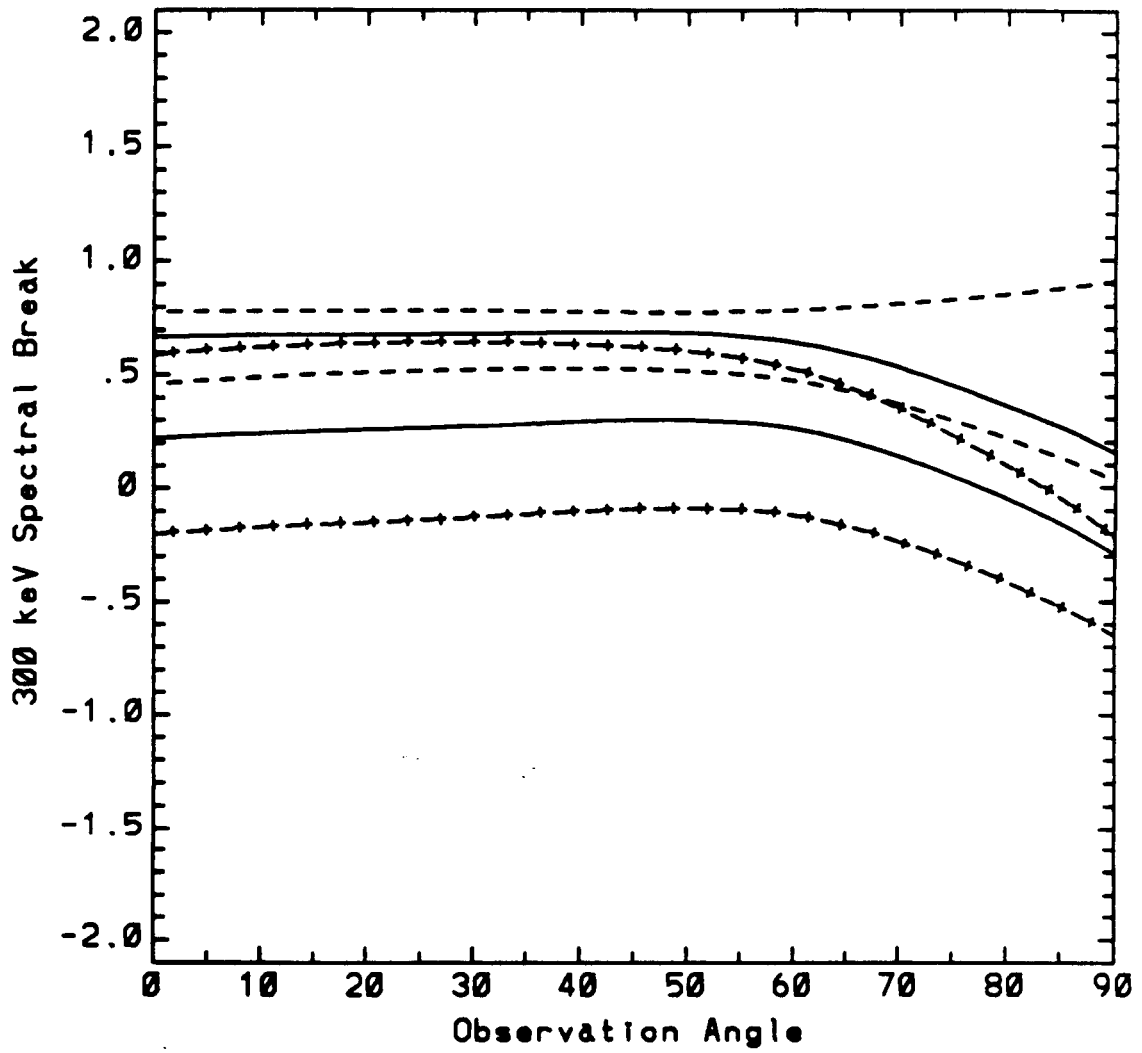
2.0
1.5
1.0
.5
0
-.5
-1.0
-1.5
-2.0
300 keV Spectral Break
0
10
20
30
40
50
60
70
80
90
Observation Angle

Figure 9

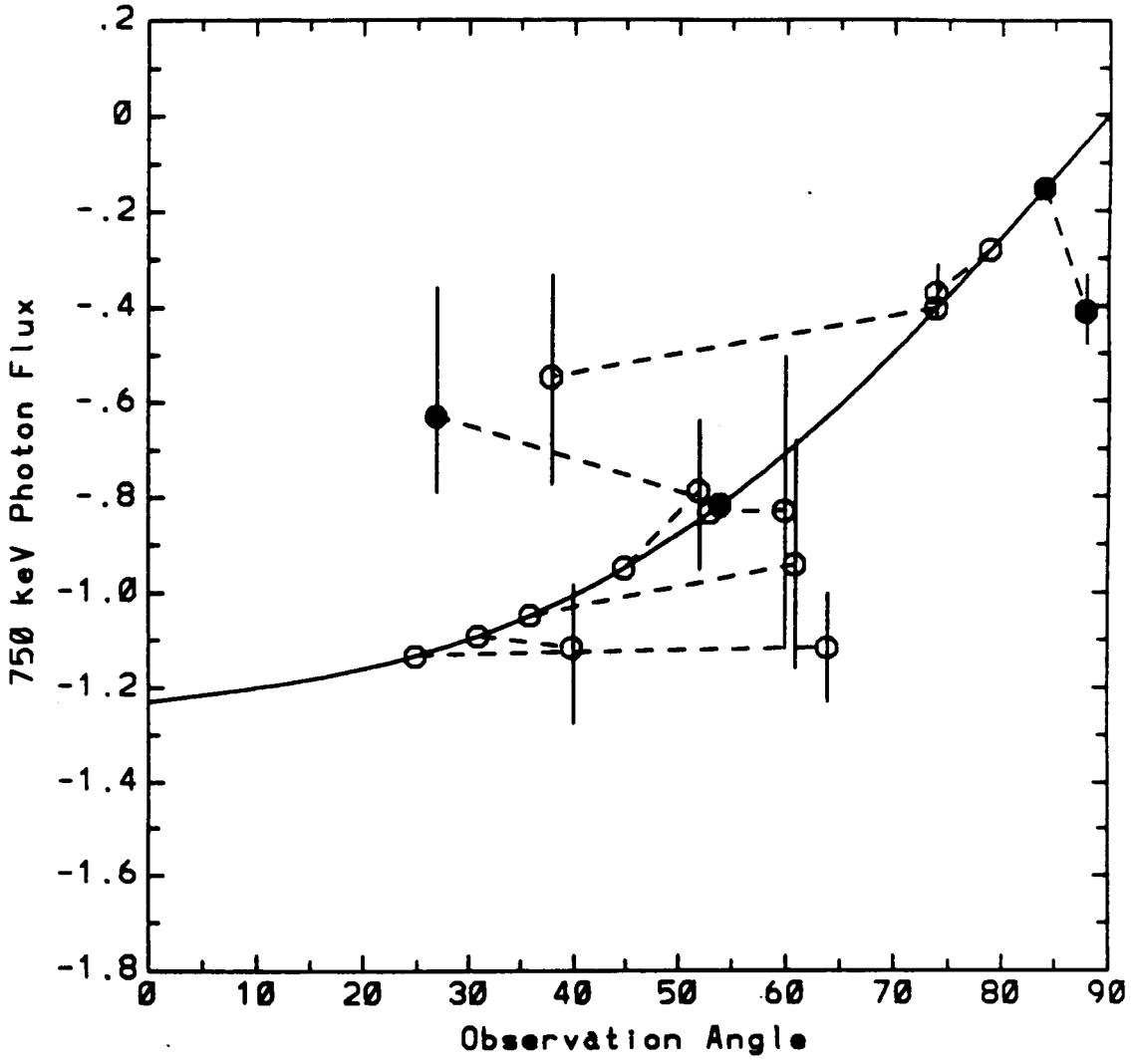
.2
0
-.2
-.4
-.6
-.8
-1.0
-1.2
-1.4
-1.6
-1.8
750 keV Photon Flux
0
10
20
30
40
50
60
70
80
90
Observation Angle

Figure 10

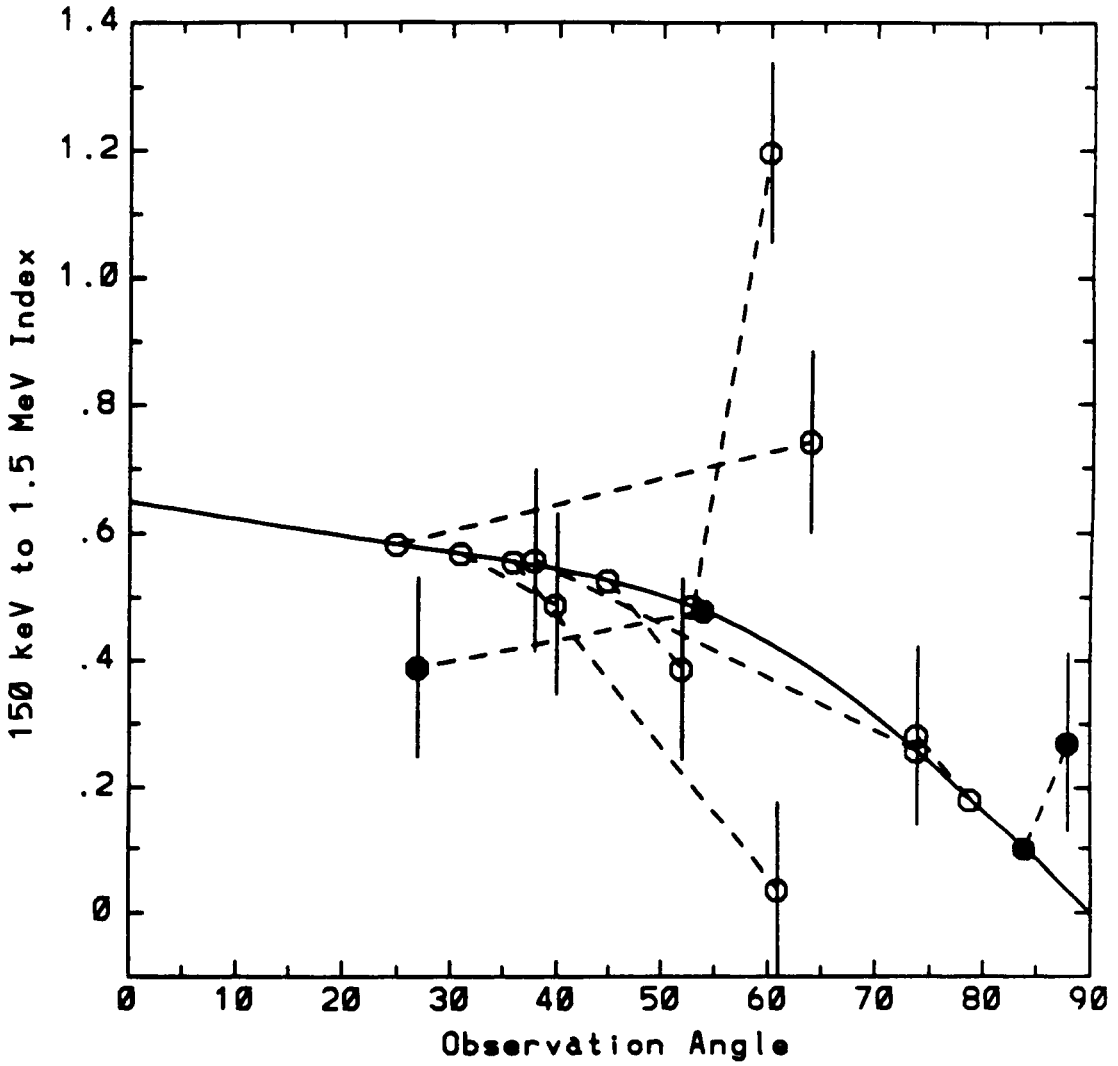
1.4
1.2
1.0
.8
.6
.4
.2
0
150 keV to 1.5 MeV Index
0
10
20
30
40
50
60
70
80
90
Observation Angle

Addresses

James M.McTiernan: Space Sciences Laboratory, University of California, Berkeley, CA 94720

Vahé Petrosian: Center for Space Science and Astrophysics, Stanford, CA 94305